



**Intercomparison of Fast airborne Ozone Instruments to measure Eddy Covariance Fluxes:
Spatial variability in deposition at the ocean surface and evidence for cloud processing**

Randall Chiu^{1,2}, Florian Obersteiner³, Alessandro Franchin⁴, Teresa Campos⁴, Adriana Bailey⁴,
5 Christopher Webster⁴, Andreas Zahn³, and Rainer Volkamer^{1,2,*}

1 Department of Chemistry, University of Colorado Boulder, 215 UCB, Boulder, CO, USA

2 Cooperative Institute for Research in Environmental Sciences (CIRES), University of Colorado
Boulder, 216 UCB, Boulder, CO, USA

3 Karlsruhe Institute of Technology, Institute of Meteorology and Climate Research (IMK),
10 Dept. ASF, Hermann-von-Helmoltz-Platz 1 D-76344 Eggenstine-Leopoldshafen, Germany

4 National Center for Atmospheric Research, P.O. Box 3000, Boulder, CO, 80307, USA

* corresponding authors: randall.chiu@colorado.edu, rainer.volkamer@colorado.edu

Abstract

15 The air-sea exchange of ozone is controlled by chemistry involving halogens, dissolved organic
carbon and sulfur in the sea surface microlayer. Calculations also indicate faster ozone photolysis
at aqueous surfaces, but the role of clouds as ozone sink is currently not well established. Fast
response ozone sensors offer opportunities to measure eddy covariance (EC) ozone fluxes in the
marine boundary layer. However, intercomparisons of fast airborne O₃ sensors, and EC O₃ fluxes
20 measured on aircraft have not been conducted before. In April 2022, the TI³GER (Technical



Innovation Into Iodine and GV aircraft Environmental Research) field campaign deployed three fast ozone sensors (gas chemiluminescence and a combination of UV absorption with coumarin chemiluminescence detection, CID) together with a fast water vapor sensor and anemometer to study iodine chemistry in the troposphere and stratosphere over Colorado and over the Pacific Ocean near Hawaii and Alaska. Here, we present an instrument comparison between the NCAR Fast O₃ instrument (FO₃, gas-phase CID) and two KIT Fast AIRborne Ozone instruments (FAIRO, UV absorption and coumarin CID). The sensors have comparable precision $<0.4\% \text{ Hz}^{-0.5}$ (0.15 ppbv $\text{Hz}^{-0.5}$), and ozone volume mixing ratios (vmr) generally agreed within 2% over a wide range of environmental conditions: $10 < \text{O}_3 < 1000$ ppbv; below detection $< \text{NO}_x < 7$ ppbv; and $2 \text{ ppmv} < \text{H}_2\text{O} < 4\% \text{ VMR}$. Both instrument designs are demonstrated to be suitable for EC flux measurements and were able to detect O₃ fluxes with exchange velocities (defined as positive for upward) as slow as $-0.010 \pm 0.004 \text{ cm s}^{-1}$, which is in the lower range of previously reported measurements. Additionally, we present two case studies: one in which the direction of ozone and water vapor fluxes were reversed ($v_{\text{O}_3} = +0.134 \pm 0.005 \text{ cm s}^{-1}$), suggesting that overhead evaporating clouds could be a strong ozone sink; and another in which ozone fluxes v_{O_3} are negative (varying by a factor of 6-10 from -0.036 ± 0.006 to $-0.003 \pm 0.004 \text{ cm s}^{-1}$), while the water vapor fluxes are consistently positive due to evaporation from the ocean surface and spatially homogeneous. Future work is needed to better understand the role of clouds as a possibly widespread sink of ozone in the remote marine boundary layer, and to elucidate possible drivers (physical, chemical, or biological) of the variability in ozone exchange velocities on fine spatial scales (~ 20 km) over remote oceans.



1. Introduction

In the troposphere, ozone is a pollutant with adverse health effects for both animals and plants. Eddy covariance (EC) is a technique that has been commonly employed to determine the fluxes of ozone to terrestrial and marine ecosystems. In terrestrial environments, EC flux measurements have been made over periods of months to years (Bauer et al., 2000; Güsten and Heinrich, 1996). Over land, uptake to soils and plant stomata are the major sink of ozone (Clifton et al., 2020; Massman et al., 1995). Consequently, previous campaigns have measured ozone fluxes over a variety of terrestrial settings including agricultural lands (Stella et al., 2011; Zhu et al., 2014; Lamaud et al., 2009; Zhu et al., 2015; Massman et al., 1995; Zhu et al., 2020), forests (Juráň et al., 2019; Finco et al., 2017; Zeller, 2002; Lamaud et al., 2002; Zeller and Nikolov, 2000; Kammer et al., 2019; Fares et al., 2014; Vermeuel et al., 2021; Altimir et al., 2006; Rannik et al., 2012), grasslands (Muller et al., 2009; Wohlfahrt et al., 2009), peatlands (El-Madany et al., 2017), and deserts (Güsten et al., 1996). Oceans account for ~1/3 of global ozone dry deposition (Ganzeveld et al., 2009). Ozone losses in the marine environment may be driven by reactions with halogens such as iodide (Saiz-Lopez et al., 2012) or with double bonds from fatty acid precursors (Chiu et al., 2017). EC flux measurements of ozone have also been performed in coastal and oceanic settings (Bariteau et al., 2010; Helmig et al., 2006; Gallagher et al., 2001) and over sea ice (Barten et al., 2023; Muller et al., 2012).

Whereas EC flux measurements of ozone are numerous, comparison studies are fewer. Ozone fluxes from EC methods have been compared to those from gradient measurements (Muller et al., 2009; Zhu et al., 2020; Loubet et al., 2013) and dynamic chamber methods (Plake et al.,



2015). However, comparisons of co-located EC flux measurements are uncommon. Aircraft
65 measurements have been performed near tower facilities (Massman et al., 1995), but ozone
fluxes at altitude may differ from those at ground level. To our knowledge, the only aircraft
instrument intercomparison for ozone EC flux was performed by Muller et al., (2010), who
measured ozone EC flux using two dry chemiluminescence instruments over grassland. The
PASE campaign flew two ozone instruments over the equatorial Pacific Ocean, but only one had
70 fast response suitable for EC flux calculation (Conley et al., 2011). Here we present the first
aircraft ozone EC flux intercomparison of three ozone instruments of two different designs over
remote marine air.

Section 2 introduces the Technological Innovation Into Iodine and GV Environmental Research
(TI³GER) field campaign, and describes the instruments and methods used to calculate fluxes of
75 O₃ and H₂O by the EC technique. Section 3 compares the O₃ concentrations and EC fluxes in
context with the available literature over oceans, assesses spatial variability and the EC flux error
budget. Finally, Section 4 summarizes the conclusions and gives an outlook for future work.

2. Methods

2.1. The TI³GER field campaign

80 In April 2022, the Technological Innovation Into Iodine and GV Environmental Research
(TI³GER) technical campaign was performed to lay the groundwork for future field
investigations into the interactions of ozone and iodine in the upper troposphere lower
stratosphere (UTLS). In total, eight research flights (RFs) were conducted, with RFs 01 and 02
over the continental United States, and RFs 03-08 conducted over the Pacific Ocean near Hawaii
85 and Alaska. Among the instruments flown on TI³GER were three ozone instruments, two of



which were of an identical design. The NCAR Fast O₃ instrument operates by NO₂ chemiluminescence and has been in use since the early 1970s (Ridley et al., 1992, 1972; Ridley and Howlett, 1974; Pearson, R. and Stedman, 1980). Two copies of the Fast AIRborne Ozone (FAIRO) instrument from KIT were also deployed (FAIRO 1 and FAIRO 2). The FAIRO
90 instruments operate by coumarin chemiluminescence calibrated against a dual-beam UV absorption photometer.

One objective of TI³GER was to compare the performance of the two instrument designs and evaluate their ability to measure EC flux of ozone on the NCAR/NSF Gulfstream 5 (GV) platform. The GV measures 3-D winds using a combination of measurements from pitot, static,
95 and radome sensors; the vertical components of these 3-D winds are needed for EC analysis. In all, EC flux measurements were performed during nineteen legs flown over the Pacific Ocean. The continental flights are not discussed here because they did not include many EC flux measurements. A table of the relevant meteorological and ocean-state variables appears in the supplement as Table S1. Figure 1 shows a map of where attempts were made to measure EC flux.
100 The arrows point to the locations of the flux legs with curves showing the five-day back-trajectories of the sampled air calculated by HYSPLIT (Stein et al., 2015; Rolph et al., 2017) using the National Oceanographic and Atmospheric Administration (NOAA) National Centers for Environmental Prediction (NCEP) Global Forecasting System (GFS) meteorological dataset.

2.2. Ozone Instrumentation

105 Three ozone instruments were installed on the GV. Two (the FAIRO instruments) were of an identical design.



2.2.1. The NCAR Fast O₃ instrument

The NCAR Fast O₃ instrument sampled from a HIAPER Modular Inlet (HIMIL). All tubing was made of Teflon. The total mass flow in the inlet was 2370 sccm. The sample line was 70 cm long
110 with an inner diameter of 6.4 mm. From this flow, Fast O₃ sampled 500 sccm through a 140 cm-long line with an inner diameter of 3.8 mm. All flows had a constant absolute pressure of 70 torr. Fast O₃ provides 10 Hz data by detecting photons from the following chemiluminescence reaction:



The excited NO₂ in R2 can also be quenched by collision with other molecules. Water vapor quenches excited NO₂ more efficiently than do nitrogen or oxygen (Matthews et al., 1977), so after time stamp synchronization among the instruments (see Sect. 2.3.), the following water vapor correction is applied (Ridley et al., 1992):

120 $[O_3]_{corrected} = [O_3] \times (1 + 4.3(\pm 0.3) \times 10^{-3} \times [H_2O]) \quad (1)$

where [O₃] is the ozone mixing ratio in ppbv, and [H₂O] is the water vapor mixing ratio in permille by volume of dry air.

The water vapor correction is performed using VCSEL water vapor data (see Sect. 2.2.) that are collected at a higher frequency (25 Hz) than are the Fast O₃ data. Thus, the water vapor
125 correction is expected to contribute negligible bias to the EC flux calculations. To assess the potential impact of the water vapor correction on Fast O₃ EC fluxes, the constant in eq. (1) was varied from its minimum and maximum estimated values (4.0 – 4.6) in the RF03-C-2 leg; the



change in this parameter resulted in biases in the EC flux results of no more than 0.7%.

Neglecting the water vapor correction altogether decreased the calculated exchange velocity (see
130 Sect. 2.4) by 5% from 0.131 cm s^{-1} to 0.124 cm s^{-1} (see Table 2). However, since the 0.131 cm s^{-1}
value is in good agreement with the EC flux results from FAIRO 1 and FAIRO 2, and since the
Fast O₃ exchange velocities are not systematically higher or lower than those from FAIRO 1 or
FAIRO 2, we believe that the water vapor correction is not a source of bias in EC flux
calculations.

135 The Fast O₃ instrument was calibrated after the campaign using a TECO Model 49i-PS ozone
primary standard. The typical instrument detection limit is $0.5 \text{ ppbv Hz}^{-0.5}$ with an accuracy not
better than 5% at high signal to noise.

2.2.2. The KIT Fast AIRborne Ozone (FAIRO) instruments

Two identical FAIRO instruments were deployed. The FAIRO instruments were independently
140 checked for proper functioning both prior to the campaign using an Ansyco (now Gasmot
Technologies) SYCOS KT-O3M and after the campaign using a TECO 49i-PS. The FAIROs
sampled from a separate HIMIL (aft-facing inlet line) through a PFA line with a length of 4.3 m
and a 1/6-inch inner diameter. Outside air was pulled at $11 \text{ vol.-L min}^{-1}$ at ambient pressure by a
Vacuubrand MD1 pump downstream of the instruments. The flow was split at a T-fitting $\sim 0.5 \text{ m}$
145 ahead of the FAIROs. Internally, $2.5 \text{ vol.-L min}^{-1}$ of flow went to the UV photometer, which
measured ozone absorption around 255 nm within the Hartley band. The O₃ absorption cross
section and temperature dependence are taken from (Barnes and Mauersberger, 1987). The UV
absorption channel operates at 0.25 Hz. A second, faster 12.5 Hz coumarin chemiluminescence
detector (CID) (Ermel et al., 2013) is calibrated against the UV channel and provides the data



150 used in EC flux calculations. The dual detector FAIRO design has two main advantages over the
Fast O₃ instrument: the FAIROs are lightweight (approx. 14 kg, 19” rack slot with 3 height units
per instrument) and do not require operating fluids such as compressed gases. Scattering by
aerosols and absorption by aromatic compounds and water vapor are well-known interferences
for UV ozone instruments (Dunlea et al., 2006). The potential for humidity changes to
155 interference with FAIRO uv photometers was further investigated, and is found to be small yet
not fully insignificant (see Supplementary Figure S1). Interference from aerosols is avoided by
the backward-facing sample inlet and aromatic compounds are expected to be minimal in the
pristine air sampled in RFs 03-07. A detailed technical description of FAIRO CID can be found
in (Zahn et al., 2012). The instrument detection limit is below 1 ppbv Hz^{-0.5} (provided by the
160 CID) and the total uncertainty 1.5% (mainly determined by the uncertainty of the O₃ absorption
cross section found in the literature) or 1.5 ppbv, whatever is lower.

2.2. Water vapor: VCSEL

Water vapor in the free stream above the GV is measured by the vertical cavity surface emitting
laser (VCSEL) hygrometer. VCSEL is an open-path optical cavity measuring two absorption
165 lines for high dynamic range: a strong line at 1854.03 nm for low vmrs and a weak line at
1853.37 nm for high vmrs. Data are collected at 25 Hz. During the flux legs, water vapor is
always above the VCSEL detection limit of 0.8 ppmv. Details about the operation of VCSEL can
be found in Zondlo et al., (2010).

2.3. Instrument time stamp synchronization

170 The three ozone instruments and the GV variables are measured on four independent time
stamps, each with its own potential offset and drift. Conveniently, ozone and water vapor vmrs



are occasionally anticorrelated (and less frequently, correlated). We use these anticorrelation events to synchronize each ozone instrument with VCSEL since VCSEL is already synchronized to the anemometer. First, the ozone and VCSEL signals are interpolated to a common 100 Hz
175 timestamp. Second, each ozone time series is visually inspected to identify unambiguous anticorrelation events with the water vapor time series in the periods before and after each flux leg. Third, the time lag at each anticorrelation event is determined by shifting the interpolated ozone signal until the absolute value of the covariance between the ozone and VCSEL signals is maximized. Finally, with the time lag identified both before and after the leg, the ozone time
180 stamp is linearly stretched to match the VCSEL time stamp.

2.4. Eddy covariance flux calculations

Eddy covariance (EC) is a commonly used technique to determine the fluxes of gases in well-mixed surface layers. Given chemical concentration and wind speed data, EC flux can be calculated as:

$$185 \quad ECflux = cov(x, w) = \frac{1}{n} \sum_{i=1}^n (x_i - \bar{x}) (w_i - \bar{w}) \quad (2)$$

where x is the concentration of the chemical species and w is the vertical wind component. For non-stationary conditions, wavelet analysis (WA) is commonly employed instead (Torrence and Compo, 1998). In WA, the time series are first transformed into a wavelet by convolution with a wavelet function:

$$190 \quad W_s(a, b) = \int_{-\infty}^{\infty} s(t) \psi_{a,b}(t) dt \quad (3)$$

$$\psi_{a,b}(t) = \frac{1}{\sqrt{a}} \psi_0 \left(\frac{t-b}{a} \right) \quad (4)$$



where a and b are translation factors for Ψ_0 , the “mother wavelet” function. For eddy covariance applications, the typical choice for the mother wavelet is the Morlet wavelet:

$$\psi_0(\eta) = \pi^{-\frac{1}{4}} e^{i\omega_0\eta} e^{-\frac{\eta^2}{2}}, \omega_0 = 6 \quad (5)$$

195 The WA flux is then calculated as $|W_w W_x|$, where W_w and W_x are the wavelet coefficients of wind and ozone, respectively (Wolfe et al., 2018).

A challenge in EC flux error analysis is that EC flux is not a measurement from a single instrument, but rather the combination of measurements from two instruments: a chemical monitor of some sort and an anemometer. For individual instruments, estimation of the limit of
200 detection (LOD) from random error (RE) can be straightforward:

$$LOD = \alpha \times \Re \quad (6)$$

where α is a dimensionless factor corresponding to the confidence level (1.96 for 95% CL, 3 for 99% CL). The standard deviation of blank measurements can be used to estimate the RE of a single instrument. However, this method is not applicable to flux measurements due to the lack
205 of true “blanks” matching the chemical and meteorological conditions of interest.

Several methods for determining the LOD of EC flux measurements have been put forth based on statistical treatments of the cross-covariance of the chemical and wind data at different time lags. For example, (Langford et al., 2015) present the following formula for estimating the root mean squared error (RE_{RMSE}):

$$210 \quad \Re_{RMSE} = \sqrt{0.5 \left((\sigma_{f_{w'c'[-\tau]}})^2 + (\overline{f_{w'c'[-\tau]}})^2 + (\sigma_{f_{w'c'[\tau]}})^2 + (\overline{f_{w'c'[\tau]}})^2 \right)} \quad (7)$$



where $\sigma_{f_{w/cr}}$ and $\overline{f_{w/cr}}$ are the standard deviation and average of the cross-covariance, and $\pm\Gamma$ represent time lags far away from the true time lag between the wind and chemical measurements. Currently, no well-established method for estimating the LOD of EC and WA fluxes is commonly accepted. The number of independent replicate measurements of ozone
215 available during TI³GER gave us the unique opportunity to explore, evaluate and optimize methods to constrain the uncertainty of EC fluxes, since the standard deviation of the fluxes measured between the individual instruments can give a sense of the magnitude of the “true” error.

A MATLAB toolkit (AirChem/FluxToolbox: Collections of scripts for eddy covariance flux
220 calculations (both traditional and wavelet-based), 2023) was used for this work. Raw data must be pre-processed to remove data gaps before inputting to the toolbox. Data gaps are removed by linear interpolation; such gaps are rare, and interpolation is used only to remove up to three or four points (out of ~2000-4000 which is typical for a flux leg). Because the GV data are recorded at higher resolution than are the ozone data, the wind and VCSEL data are binned to each ozone
225 instrument’s corrected time stamp.

For EC fluxes, the toolbox detrends the data with a boxcar method in a user-defined time frame. The lengths of the detrending time frames were selected to balance being short enough to remove systematic cross-covariance structures with being long enough to retain low-frequency fluxes. A detrending time of 10 s was used in all fluxes presented below. At typical aircraft speeds, 10 s
230 corresponds to 1-1.2 km. In addition to calculating an eddy covariance flux, the toolbox also calculates WA flux (Torrence and Compo, 1998) and outputs cospectra as a function of frequency.



In contrast to common practice, we express ozone fluxes in terms of exchange velocity (v_e) rather than deposition velocity (v_d), where:

$$235 \quad v_e = \frac{\text{flux}(\text{ppbms}^{-1})}{\text{concentration}(\text{ppb})} \times \frac{100\text{cm}}{1\text{m}} \quad (8)$$

Exchange velocity is the same as deposition velocity apart from the lack of a negative sign, i.e. upward directed fluxes have positive v_e . We use v_e rather than v_d because some interesting case studies presented have upward directed fluxes, which are more intuitively represented using positive signs.

240 Notably, fluxes and cross-covariances in principle have the same units ($\text{molec cm}^{-2} \text{s}^{-1}$ or ppb m s^{-1}). However, we use "covariance" to refer to the cross-covariance calculated for different lag times by our code, and "flux" to identify an atmospheric state. This distinction is useful when discussing EC flux errors, which are estimated from cross-covariances at time lags departing from the true lag between instruments. Whereas such cross-covariances represent true statistical
245 covariance, they do not represent atmospheric fluxes.



3. Results and Discussion

3.1. Instrument intercomparison

Figure 2 shows the time series of O₃ from all three sensors from RF03 as an example. Panel A shows the altitude of the GV, and Panel B shows the water vapor and ozone time series for the entire flight. Water vapor/ozone time synchronization was performed as close to the beginning and the end of the flight as correlation events could be visually identified; close-ups of these events are shown in Panels C and E. For EC flux legs, time synchronization was performed before and after each leg rather than for the entire flight. Before the covariance synchronization, the ozone time stamps differed from the VCSEL time stamp by up to five seconds. The beginning and end close-ups show that the synchronization procedure matches the signals to within ± 0.1 s. However, Panel D shows that the ozone signals are not synchronized with each other or to a water vapor correlation event midway through the flight. The discrepancy could be caused by a combination of different flow conditions at different altitudes or instrumental clock drift. However, because the FAIRO instruments share an inlet line that forks only in the last ~ 0.5 m, inlet line flow differences alone cannot explain their time offset. Inspection of the delays from each RF show that the ozone clocks drift no more than ± 0.7 s (typically ≤ 0.5 s). For ozone instrument comparisons, data were averaged over 10 s to prevent bias from synchronization errors.

Aggregated data from RF03-07 are shown in Figure 3, Panel A. Ozone vmrs measured by each FAIRO are plotted against ozone vmrs measured by Fast O₃. Linear fits of the FAIRO vmrs are also shown. The data from both instrument designs appear to be linear, with a 2% overall difference.



In Panels B-D, the absolute and relative differences between each instrument and the average of all three instruments are shown (see Fig. 3). In all cases, data are color-coded for high water vapor (concentration $> 1.4 \times 10^{17}$ molec cm⁻³, blue) and high NO_x (volume mixing ratio > 200 pptv, red). GPS altitude, VCSEL water vapor concentration, and NO_x are also shown in the background of Panels B, C, and D, respectively, for context. Neither the absolute nor the relative differences from the average exhibit systematic behavior depending on water vapor or NO_x. The effect of humidity changes did not reveal any obvious explanation for O₃ differences when comparing individual instruments to the instrument mean (not shown; for the effect of changing humidity when comparing FAIRO instruments, see Supplementary Figure S1). Although the persistent differences from average are accompanied by high NO_x conditions between ~00:00-02:00 on 21 April 2022 UTC, high NO_x conditions between ~19:30-20:00 on 20 April 2022 UTC are not accompanied by similar differences. High water vapor during a low-altitude flux leg at 21:00 UTC is accompanied by agreement amongst all three instruments within 2%.

The agreement of the instruments was also evaluated individually for RFs 03-07. The fit results for each flight are shown in Table 1.

A subset of flux legs with low ozone variability was used to infer an upper limit of the precision of each instrument, as the contribution by additional atmospheric variability can't be fully eliminated. The ozone time series from each flux leg is smoothed over one second and the range is calculated of the smoothed data. Variability is calculated as the relative range of ozone in that leg. Flux legs are characterized as low-variability if the relative range of the smoothed time series is less than 5% for at least two instruments. Precision is calculated as the standard deviation of the unsmoothed time series. All three instruments have comparable precision, with



290 Fast O₃ precision at 1.4% (0.45 ppb) at 10 Hz, FAIRO 1 at 1.2% (0.36 ppb) at 12.5 Hz, and
FAIRO 2 at 1.1% (0.36 ppb) at 12.5 Hz. These precision estimates represent an upper bound as
some of the variability could be true atmospheric variability. More detail on the precision
calculations can be found in Table S2 of the supplement.

3.2. Eddy covariance flux

295 Potential temperature (Θ) and equivalent potential temperature (Θ_e) profiles are used to
determine whether flux legs were conducted within the MBL. Example profiles are shown in
Figure 4.

The profiles shown are taken from both descent and ascent except in the case of the RF03-C flux
legs, which were performed as the plane approached the airport for landing. The flux legs in
300 RF04 were conducted over the tropical Pacific Ocean, and both profiles indicate an MBL height
of ~800 m. The utility of Θ_e in determining the MBL height is evident in the RF06-A legs, which
were conducted off the coast of Alaska. The Θ profile on the descent does not unambiguously
show an MBL height, but the Θ_e profile clearly indicates an MBL height of ~200 m on both the
descent and ascent. Such a shallow MBL near the Kenai Fjords combined with the strong
305 temperature inversion suggests RF06-A may be subject to distinct "pools" of air; yet the Θ_e
profiles suggest mixing to the surface. The MBL height in RF03-A is difficult to distinguish and
may be ~500 m. In all cases, flux legs were conducted at heights well within the MBL except in
RF03, where flux legs were conducted at 107, 476, and 889 m.

The time delay between VCSEL and the wind data is determined by calculating the water vapor
310 flux. VCSEL and wind speed data are well-synchronized; in most (12) cases, the water vapor
cross-covariance had a peak at a time lag of zero points; in six cases the optimal lag was -1 point



on the 12.5 Hz FAIRO time stamp (within 0.08 s). In one case (RF07-A-4) the VCSEL cross-covariance peaked at +5 points, but this is likely a spurious correlation because the VCSEL data from the previous leg was well-synchronized (zero time lag).

315 Because water vapor fluxes are strong and always above detection, the VCSEL/wind time offset allows us to anchor the ozone time offset and limit our search for an ozone covariance peak to ± 0.7 s from the VCSEL time offset since that is the maximum observed ozone/VCSEL time delay. An ozone flux is reported for an instrument only if a cross-covariance peak is found within that window. A flux is not reported for an instrument if the covariance behavior within that

320 window is primarily one of sign-change, e.g. if the covariance linearly increases from negative to positive, or if there are many zero-crossings. If all three instruments show a covariance that survives this filter, then an average flux is reported for that leg. Of the 19 flux legs, 11 had fluxes that met this criterion, and are summarized in Table 2. A full version of Table 2 with meteorological conditions and other compounds of interest is included in the Supplementary

325 Information.

3.3. Comparison with literature

A previous study has compared ozone EC flux measurements from dry chemiluminescence ozone instruments over grassland (Muller et al., 2010), but to our knowledge no instrument intercomparisons have been performed on board aircraft. Aircraft measurements of ozone flux

330 have been reported before over land (Wolfe et al., 2018, 2015; Lenschow et al., 1980) and over the ocean during PASE (Conley et al., 2011). In the latter, ozone exchange velocities were -0.024 ± 0.014 cm s⁻¹. Larger data sets for marine ozone flux have been produced by ship campaigns. The TexAQS cruise reported ozone exchange velocities as large as -0.81 ± 0.27



cm s⁻¹ in coastal channels and -0.034 ± 0.003 cm s⁻¹ in offshore areas, and the STRATUS cruise
335 measured -0.009 ± 0.001 cm s⁻¹ over open ocean areas (Bariteau et al., 2010; Helmig et al.,
2006). All three instruments tested here can detect exchange velocities in the lower range
observed in the remote ocean.

3.4. Constraining the error estimate

Figure 5 shows three examples of covariance plots from flux legs that are representative of the
340 range of conditions observed. Ozone plots are shown on the left, and the corresponding plots for
VCSEL are shown on the right. For all cross-covariances, the Langford LOD is calculated by
using $\Gamma = 30$ s at the beginning and end of the cross-covariance plot, and the Langford 99% CL
LOD for Fast O3 is shown as a light gray shading. Panel A (RF03-C-2) is a case in which all
three ozone instruments measured an upward directed flux and VCSEL (Panel F) shows water
345 vapor directed downward toward the ocean; this case is described in more detail below. Panel B
(RF04-A-1) shows ozone depositing into the ocean and water vapor evaporating out of the
ocean. These two cases are examples of EC flux strong enough to be unambiguously identified
by all three ozone instruments, i.e. that each instrument's flux measurement is above the LOD as
defined by Langford et al. (2015).

350 Panel C (RF06-A-1) shows a case in which no ozone instrument derived flux is above the
Langford LOD. Viewed in isolation, no instrument's cross-covariance is convincing on its own.
However, a small candidate peak can be identified within the ± 0.5 s interval.

The average exchange velocity measured by all three instruments in RF06-A-1 is -0.010 cm s⁻¹
with a standard deviation of 0.004 cm s⁻¹. The Langford RE_{RMSE} for this leg corresponds to
355 0.0057 - 0.0074 cm s⁻¹ depending on the instrument and thus overstates the error and LOD. We



propose a modification of the Langford approach by restricting the interval Γ by calculating the integral time scale. The integral time scale τ characterizes the period over which covariance persists. We estimate τ by integrating outward from the peak until the integral crosses zero (Lenschow et al., 2000). It is possible in certain cases for the calculation of τ to fail. This
360 happened for the VCSEL data shown in Panel H (RF06-A-1). In this case τ was estimated as the width between the second zero-crossings from the peak.

We then apply the Langford RE_{RMSE} calculation to intervals $+\Gamma$ and $-\Gamma$ which are τ in length and are centered around relatively smooth areas of cross-correlation near the candidate peak. The 99% LOD calculated in this modified approach is shown in Figure 5 as dark gray shading. The
365 RE_{RMSE} estimated by the modified approach corresponds to 0.0053-0.0064 cm s^{-1} , which is more in line with the “true” random error among the three measurements.

3.5. Spatial variability of ozone and water vapor fluxes

The fluxes of ozone and water vapor were in the counterintuitive directions during the RF03-C legs. Water vapor was carried downwards, although the ocean surface is usually a water vapor
370 source by evaporation. Conversely, ozone was carried upwards, even though the ocean surface is expected to be an ozone sink. The ozone exchange velocity in this leg (RF03-C-2) was +0.134 cm s^{-1} measured at an altitude of 889 m. At a lower altitude of 476 m, (RF03-C-3), the exchange velocity was +0.097 cm s^{-1} . These velocities are consistent with the lower range of nocturnal entrainment velocities (0.12 – 0.72 cm s^{-1}) measured during the DYCOMS-II campaign over the
375 Eastern Pacific Ocean (Faloona et al., 2005). However, entrainment cannot explain these fluxes because the air above the plane was dryer, as can be seen from the profiles in Figure 6.



A plausible source of water vapor above the plane is evaporating cloud droplets; indeed, footage from this RF shows the plane flying below numerous low clouds. RF03-C took place near solar noon, so the NO_2 photolysis frequency (J_{NO_2}) measured by the HIAPER Airborne Radiation
380 Package (HARP) actinic flux instrument can be used as a proxy for overhead cloudiness (see top panel of Figure 6). A period of high ozone and water vapor flux between 22:41 and 22:43 UTC is accompanied by oscillations in J_{NO_2} that indicate heavy cloud cover. Stills from the flight movies are shown in Figure 7.

In the left panel of Figure 7, the forward- and side- looking cameras show light high-altitude
385 clouds corresponding to a time (22:39:59 UTC) of low J_{NO_2} variability and fluxes near zero for both ozone and water vapor. The right panels show the same views with heavy low clouds visible, corresponding to a time (22:41:57 UTC) when the J_{NO_2} variability is high, water vapor flux is toward the ocean, and ozone flux is toward the clouds above.

We hypothesize that evaporating clouds provide a source of water vapor while simultaneously
390 providing a sink of ozone. Previously, it was proposed that an increase in aqueous phase chemistry in cloud droplets would decrease ozone production in high- NO_x environments and enhance ozone destruction in low- NO_x environments (Lelieveld and Crutzen, 1990).

Computational simulations suggest that ozone could be stabilized within the air-water interface (within the first 4 Å), and that modification of the ozone UV-vis absorption cross section and
395 activation of photolytic pathways at the interface can increase the ozone photolysis rate constant by more than a factor of 20 (Anglada et al., 2014). The observations from the RF03-C legs may represent the first field evidence of these proposed processes. Critically, the RF03-C-1 flux leg performed at 107 m immediately prior to the RF03-C-2 887 m leg found fluxes below detection



for all three ozone instruments. Thus, if cloud effects are operative, they may well be invisible to
400 surface-based platforms such as ships.

Compared to shipborne measurements taken over the course of days or weeks, the flux legs here
are necessarily shorter, with the longest leg being ten minutes and the legs being only ~5 minutes
long on average. To assess the consistency between sensors on shorter time scales, the ozone EC
fluxes were also calculated in 75-second long quarters for the flux example RF06-A-1 shown in
405 Figure 7.

The ozone flux observed in this leg is carried in the first, third, and last quarters, with flux in the
second quarter below detection. However, the water vapor flux is above detection in all segments
and exhibits different trends from the ozone flux. Since the water vapor and ozone are both
carried by the same eddies, the difference in behavior cannot be attributed to meteorology.
410 Rather, the ozone flux variability must reflect true heterogeneity in the ocean and/or atmospheric
chemical states. Assuming chemical measurements are available on similar time scales, the
ozone flux can help characterize atmospheric chemistry on ~10 km spatial scales. For measuring
average fluxes, we recommend flying multiple flux legs over regions of interest for better
statistics as ozone fluxes are often near the LOD.

415 4. Conclusions and Outlook

In the aggregate, Fast O₃ and FAIRO instruments operate at comparable frequencies (10 vs 12.5
Hz data rate; 3 Hz practical resolution estimated from the mixing time of zero-air puffs at the
Fast O₃ inlet), are accurate within 2%, and have similar LOD at their typical sampling rates (1.5
ppbv). Large excursions in measured ozone vmrs (of up to 30%, or 5 ppbv difference) are
420 sometimes observed in the ratio of high-rate data between the instruments, but the excursions



show no systematic behavior with respect to ozone concentration, water vapor or NO_x. These differences did not occur during the flux legs. From an operational standpoint, the FAIRO design is advantageous, because the instrument and pump fit into a single 19” rack and requires no hazardous NO gas.

425 Simultaneous, high-frequency H₂O measurements in the free stream are essential for synchronizing the O₃ sensors and wind measurements, and provide context to the interpretation of O₃ EC fluxes. Inlet line delays, clock drifts, and small inaccuracies in clock synchronizations lead to time offsets that are difficult to characterize with certainty. Correlation events between water vapor and ozone present direct means for clock synchronization. In principle, an ozone
430 time lag could be prescribed by matching the ozone time stamp to the water vapor time stamp and searching for time lag at which water vapor flux peaks since the water vapor flux is always above detection. In practice, clock drifts still necessitate a search for a cross-covariance peak in the ozone flux, albeit in a constrained time window.

The availability of three ozone instruments during T³GER allowed for the estimation of the
435 “true” LOD of the ozone flux (LOD_{ECflux}) using the standard deviation of the EC fluxes measured by each instrument. We use this information to provide a modified procedure to estimate error and LOD_{ECflux}: the R_{ERMSE} formula (eq. 7) (Langford et al. 2015) is combined with the concept of “integral time scale” (Lenschow et al., 2000). We find that the “true” LOD_{ECflux} (defined as the 95% CI on the mean EC flux) is overestimated by the EC flux
440 uncertainty on an individual sensor when Γ is a large time window (30 sec, as used in Lenschow et al.). Estimating the R_{ERMSE} over a smaller time window shrinks the RM_{RMSE}, and brings the EC flux uncertainty closer to the “true” error inferred from the EC flux standard deviation of



three separate sensors, without underestimating the EC flux error. We find that the integral time scale Γ suitable to estimate error is usually a few seconds, and define it here as Γ found by
445 integrating outward from a candidate covariance peak until the first zero-crossing of the covariance integral. Typical LODs for O_3 exchange velocities are 30-50% lower with shorter Γ , with typical LOD $\sim 0.005 \text{ cm s}^{-1}$, limited by spurious covariance peaks that are clearly non-physical as they exceed the believable bounds of instrument synchronization.

Ozone EC fluxes measured from aircraft in the remote MBL can exhibit significant time
450 variability on the order of minutes (6-10 km). A similar variability is not seen in the H_2O EC fluxes. While the H_2O EC fluxes are spatially more homogeneous, and de-facto constant (within 25%), a variability in the O_3 EC fluxes of larger than 600% is observed and highly significant (above $6\text{-}\sigma$ to below detection) on spatial scales of 20 km. This variability is seen consistently by all three sensors over the open ocean environments probed here. Cloud cover can reverse the
455 direction of the O_3 and H_2O fluxes, indicating a source of water vapor and a sink for O_3 above the aircraft, consistent with webcam images of clouds. The drivers of the horizontal variability in O_3 EC fluxes directed into the ocean on fine spatial scales is currently not well understood, but could relate to changes in overhead cloud cover, as well as possibly variability in ocean and atmospheric states. Future studies are needed, and would benefit from repeat legs, and
460 measurements of ocean state variables. can reverse the direction of the O_3 and H_2O fluxes, indicating a source of water vapor and a sink for O_3 above the aircraft, consistent with webcam images of clouds. The drivers of the horizontal variability in O_3 EC fluxes directed into the ocean on fine spatial scales is currently not well understood, but could relate to changes in overhead cloud cover, as well as possibly variability in ocean and atmospheric states. Future studies are
465 needed, and would benefit from repeat legs, and measurements of ocean state variables.



Code Availability

The MATLAB flux toolbox is available at: <https://github.com/AirChem/FluxToolbox>.

Data Availability

All data used in this paper can be found on the TI³GER field catalog, which is available at the
470 following URL: https://www.eol.ucar.edu/field_projects/ti3ger.

Author Contributions

RV designed the TI³GER project, and as mission scientist planned and led research flights. RC
performed data analysis of the EC fluxes and instrument intercomparison, assisted with
instrument calibrations and uninstallation, and led the manuscript preparation. FO and AZ
475 calibrated and deployed the FAIRO instruments and provided the FAIRO data. AF and TC
calibrated and deployed the Fast O₃ instrument and provided Fast O₃ data. AR and CW
calibrated the wind measurements and provided GV data. RC and RV wrote the manuscript, with
contributions from all co-authors.

Competing Interests

480 At least one of the (co-)authors is a member of the editorial board of Atmospheric Measurement
Techniques.



Acknowledgements

Financial support for TI³GER from US National Science Foundation award AGS-2027252 (PI: R. Volkamer) is gratefully acknowledged. RC and RV thank Glenn Wolfe, Erin Delaria and
485 Reem Hannun, and Dongwook Kim for helpful discussions. TI³GER was supported by the National Center for Atmospheric Research, which is a major facility sponsored by the NSF under Cooperative Agreement no. 1852977. The data were collected using NSF's Lower Atmosphere Observing Facilities, which are managed and operated by NCAR's Earth Observing Laboratory. The GV aircraft was operated by the National Center for Atmospheric Research (NCAR) Earth
490 Observing Laboratory's (EOL) Research Aviation Facility (RAF). The NCAR ozone measurements were funded by NSF Lower Atmosphere Observing Facilities and NSF NCAR/Facilities programs.

References

- 495 Altimir, N., Kolari, P., Tuovinen, J.-P., Vesala, T., Bäck, J., Suni, T., Kulmala, M., and Hari, P.: Foliage surface ozone deposition: a role for surface moisture?, *Biogeosciences*, 3, 209–228, <https://doi.org/10.5194/BG-3-209-2006>, 2006.
- Anglada, J. M., Martins-Costa, M., Ruiz-López, M. F., and Francisco, J. S.: Spectroscopic signatures of ozone at the air-water interface and photochemistry implications, *Proc Natl Acad Sci U S A*, 111, 11618–11623, <https://doi.org/10.1073/pnas.1411727111>, 2014.
500
- Bariteau, L., Helmig, D., Fairall, C. W., Hare, J. E., Hueber, J., and Lang, E. K.: Determination of oceanic ozone deposition by ship-borne eddy covariance flux measurements, *Atmos Meas Tech*, 3, 441–455, <https://doi.org/10.5194/amt-3-441-2010>, 2010.
- Barnes, J. and Mauersberger, K.: Temperature dependence of the ozone absorption cross section at the 253.7-nm mercury line, *Journal of Geophysical Research: Atmospheres*, 92, 14861–14864, <https://doi.org/10.1029/JD092ID12P14861>, 1987.
505
- Barten, J. G. M., Ganzeveld, L. N., Steeneveld, G. J., Blomquist, B. W., Angot, H., Archer, S. D., Bariteau, L., Beck, I., Boyer, M., von der Gathen, P., Helmig, D., Howard, D., Hueber, J., Jacobi, H. W., Jokinen, T., Laurila, T., Posman, K. M., Quéléver, L., Schmale, J., Shupe, M. D., and Krol, M. C.: Low ozone dry deposition rates to sea ice during the MOSAiC
510



- field campaign: Implications for the Arctic boundary layer ozone budget, *Elementa*, 11, <https://doi.org/10.1525/ELEMENTA.2022.00086/195276>, 2023.
- 515 Bauer, M. R., Hultman, N. E., Panek, J. A., and Goldstein, A. H.: Ozone deposition to a ponderosa pine plantation in the Sierra Nevada Mountains (CA): A comparison of two different climatic years, *Journal of Geophysical Research: Atmospheres*, 105, 22123–22136, <https://doi.org/10.1029/2000JD900168>, 2000.
- 520 Chiu, R., Tinel, L., Gonzalez, L., Ciuraru, R., Bernard, F., George, C., and Volkamer, R.: UV photochemistry of carboxylic acids at the air-sea boundary: A relevant source of glyoxal and other oxygenated VOC in the marine atmosphere, *Geophys Res Lett*, 44, 1079–1087, <https://doi.org/10.1002/2016GL071240>, 2017.
- 525 Clifton, O. E., Fiore, A. M., Massman, W. J., Baublitz, C. B., Coyle, M., Emberson, L., Fares, S., Farmer, D. K., Gentine, P., Gerosa, G., Guenther, A. B., Helmig, D., Lombardozzi, D. L., Munger, J. W., Patton, E. G., Pusede, S. E., Schwede, D. B., Silva, S. J., Sörgel, M., Steiner, A. L., and Tai, A. P. K.: Dry Deposition of Ozone Over Land: Processes, Measurement, and Modeling, *Reviews of Geophysics*, 58, e2019RG000670, <https://doi.org/10.1029/2019RG000670>, 2020.
- 530 Conley, S. A., Faloon, I. C., Lenschow, D. H., Campos, T., Heizer, C., Weinheimer, A., Cantrell, C. A., Mauldin, R. L., Hornbrook, R. S., Pollack, I., and Bandy, A.: A complete dynamical ozone budget measured in the tropical marine boundary layer during PASE, *J Atmos Chem*, 68, 55–70, <https://doi.org/10.1007/s10874-011-9195-0>, 2011.
- 535 Dunlea, E. J., Herndon, S. C., Nelson, D. D., Volkamer, R. M., Lamb, B. K., Allwine, E. J., Grutter, M., Ramos Villegas, C. R., Marquez, C., Blanco, S., Cardenas, B., Kolb, C. E., Molina, L. T., and Molina, M. J.: Technical note: Evaluation of standard ultraviolet absorption ozone monitors in a polluted urban environment, *Atmos. Chem. Phys*, 6, 3163–3180, 2006.
- El-Madany, T. S., Niklasch, K., and Klemm, O.: Stomatal and Non-Stomatal Turbulent Deposition Flux of Ozone to a Managed Peatland, *Atmosphere* 2017, Vol. 8, Page 175, 8, 175, <https://doi.org/10.3390/ATMOS8090175>, 2017.
- 540 Ermel, M., Oswald, R., Mayer, J. C., Moravek, A., Song, G., Beck, M., Meixner, F. X., and Trebs, I.: Preparation methods to optimize the performance of sensor discs for fast chemiluminescence ozone analyzers, *Environ Sci Technol*, 47, 1930–1936, https://doi.org/10.1021/ES3040363/SUPPL_FILE/ES3040363_SI_001.PDF, 2013.
- 545 Faloon, I., Lenschow, D. H., Campos, T., Stevens, B., van Zanten, M., Blomquist, B., Thornton, D., Bandy, A., and Gerber, H.: Observations of Entrainment in Eastern Pacific Marine Stratocumulus Using Three Conserved Scalars, *J Atmos Sci*, 62, 3268–3285, <https://doi.org/10.1175/JAS3541.1>, 2005.



- 550 Fares, S., Savi, F., Muller, J., Matteucci, G., and Paoletti, E.: Simultaneous measurements of above and below canopy ozone fluxes help partitioning ozone deposition between its various sinks in a Mediterranean Oak Forest, *Agric For Meteorol*, 198–199, 181–191, <https://doi.org/10.1016/J.AGRFORMET.2014.08.014>, 2014.
- Finco, A., Marzuoli, R., Chiesa, M., and Gerosa, G.: Ozone risk assessment for an Alpine larch forest in two vegetative seasons with different approaches: comparison of POD1 and AOT40, *Environmental Science and Pollution Research*, 24, 26238–26248, <https://doi.org/10.1007/S11356-017-9301-1/FIGURES/6>, 2017.
- 555 Gallagher, M. W., Beswick, K. M., and Coe, H.: Ozone deposition to coastal waters, *Quarterly Journal of the Royal Meteorological Society*, 127, 539–558, <https://doi.org/10.1002/QJ.49712757215>, 2001.
- 560 Ganzeveld, L., Helmig, D., Fairall, C. W., Hare, J., and Pozzer, A.: Atmosphere-ocean ozone exchange: A global modeling study of biogeochemical, atmospheric, and waterside turbulence dependencies, *Global Biogeochem. Cycles*, 23, 4021, <https://doi.org/10.1029/2008GB003301>, 2009.
- 565 Güsten, H. and Heinrich, G.: On-line measurements of ozone surface fluxes: Part I. Methodology and instrumentation, *Atmos Environ*, 30, 897–909, [https://doi.org/10.1016/1352-2310\(95\)00269-3](https://doi.org/10.1016/1352-2310(95)00269-3), 1996.
- Güsten, H., Heinrich, G., Mönnich, E., Sprung, D., Weppner, J., Ramadan, A. B., Ezz El-Din, M. R. M., Ahmed, D. M., and Hassan, G. K. Y.: On-line measurements of ozone surface fluxes: Part II. Surface-level ozone fluxes onto the Sahara desert, *Atmos Environ*, 30, 911–918, [https://doi.org/10.1016/1352-2310\(95\)00270-7](https://doi.org/10.1016/1352-2310(95)00270-7), 1996.
- 570 Helmig, D., Lang, E. K., Bariteau, L., Boylan, P., Fairall, C. W., Ganzeveld, L., Hare, J. E., Hueber, J., and Pallandt, M.: Atmosphere-ocean ozone fluxes during the TexAQS 2006, STRATUS 2006, GOMECC 2007, GasEx 2008, and AMMA 2008 cruises, *Journal of Geophysical Research: Atmospheres*, 117, <https://doi.org/10.1029/2011JD015955>, 2006.
- 575 Juráň, S., Šigut, L., Holub, P., Fares, S., Klem, K., Grace, J., and Urban, O.: Ozone flux and ozone deposition in a mountain spruce forest are modulated by sky conditions, *Science of The Total Environment*, 672, 296–304, <https://doi.org/10.1016/J.SCITOTENV.2019.03.491>, 2019.
- 580 Kammer, J., Lamaud, E., Bonnefond, J. M., Garrigou, D., Flaud, P. M., Perraudin, E., and Villenave, E.: Ozone production in a maritime pine forest in water-stressed conditions, *Atmos Environ*, 197, 131–140, <https://doi.org/10.1016/J.ATMOSENV.2018.10.021>, 2019.



- Lamaud, E., Carrara, A., Brunet, Y., Lopez, A., and Druilhet, A.: Ozone fluxes above and within a pine forest canopy in dry and wet conditions, *Atmos Environ*, 36, 77–88, [https://doi.org/10.1016/S1352-2310\(01\)00468-X](https://doi.org/10.1016/S1352-2310(01)00468-X), 2002.
- 585 Lamaud, E., Loubet, B., Irvine, M., Stella, P., Personne, E., and Cellier, P.: Partitioning of ozone deposition over a developed maize crop between stomatal and non-stomatal uptakes, using eddy-covariance flux measurements and modelling, *Agric For Meteorol*, 149, 1385–1396, <https://doi.org/10.1016/J.AGRFORMET.2009.03.017>, 2009.
- 590 Langford, B., Acton, W., Ammann, C., Valach, A., and Nemitz, E.: Eddy-covariance data with low signal-to-noise ratio: Time-lag determination, uncertainties and limit of detection, *Atmos Meas Tech*, 8, 4197–4213, <https://doi.org/10.5194/AMT-8-4197-2015>, 2015.
- Lelieveld, J. and Crutzen, P. J.: Influences of cloud photochemical processes on tropospheric ozone, *Nature*, 343, 227–233, <https://doi.org/10.1038/343227a0>, 1990.
- 595 Lenschow, D. H., Delany, A. C., Stankov, B. B., and Stedman, D. H.: Airborne measurements of the vertical flux of ozone in the boundary layer, *Boundary Layer Meteorol*, 19, 249–265, <https://doi.org/10.1007/BF00117223>/METRICS, 1980.
- Lenschow, D. H., Wulfmeyer, V., and Senff, C.: Measuring Second-through Fourth-Order Moments in Noisy Data, *J Atmos Ocean Technol*, 17, 1330–1347, [https://doi.org/https://doi.org/10.1175/1520-0426\(2000\)017<1330:MSTFOM>2.0.CO;2](https://doi.org/https://doi.org/10.1175/1520-0426(2000)017<1330:MSTFOM>2.0.CO;2),
600 2000.
- Loubet, B., Cellier, P., Fléchar, C., Zurfluh, O., Irvine, M., Lamaud, E., Stella, P., Roche, R., Durand, B., Flura, D., Masson, S., Laville, P., Garrigou, D., Personne, E., Chelle, M., and Castell, J. F.: Investigating discrepancies in heat, CO₂ fluxes and O₃ deposition velocity over maize as measured by the eddy-covariance and the aerodynamic gradient methods,
605 *Agric For Meteorol*, 169, 35–50, <https://doi.org/10.1016/J.AGRFORMET.2012.09.010>, 2013.
- Massman, W. J., Macpherson, J. I., Delany, A., Den Hartog, G., Neumann, H. H., Oncley, S. P., Pearson, R., Pederson, J., and Shaw, R. H.: Surface conductances for ozone uptake derived from aircraft eddy correlation data, *Atmos Environ*, 29, 3181–3188,
610 [https://doi.org/10.1016/1352-2310\(94\)00330-N](https://doi.org/10.1016/1352-2310(94)00330-N), 1995.
- Matthews, R. D., Sawyer, R. F., and Schefer, R. W.: Interferences in chemiluminescent measurement of nitric oxide and nitrogen dioxide emissions from combustion systems, *Environ Sci Technol*, 11, 1092–1096, <https://doi.org/10.1021/es60135a005>, 1977.
- 615 Muller, J. B. A., Coyle, M., Fowler, D., Gallagher, M. W., Nemitz, E. G., and Perciva, C. J.: Comparison of ozone fluxes over grassland by gradient and eddy covariance technique, *Atmospheric Science Letters*, 10, 164–169, <https://doi.org/10.1002/ASL.226>, 2009.
- Muller, J. B. A., Percival, C. J., Gallagher, M. W., Fowler, D., Coyle, M., and Nemitz, E.: Sources of uncertainty in eddy covariance ozone flux measurements made by dry



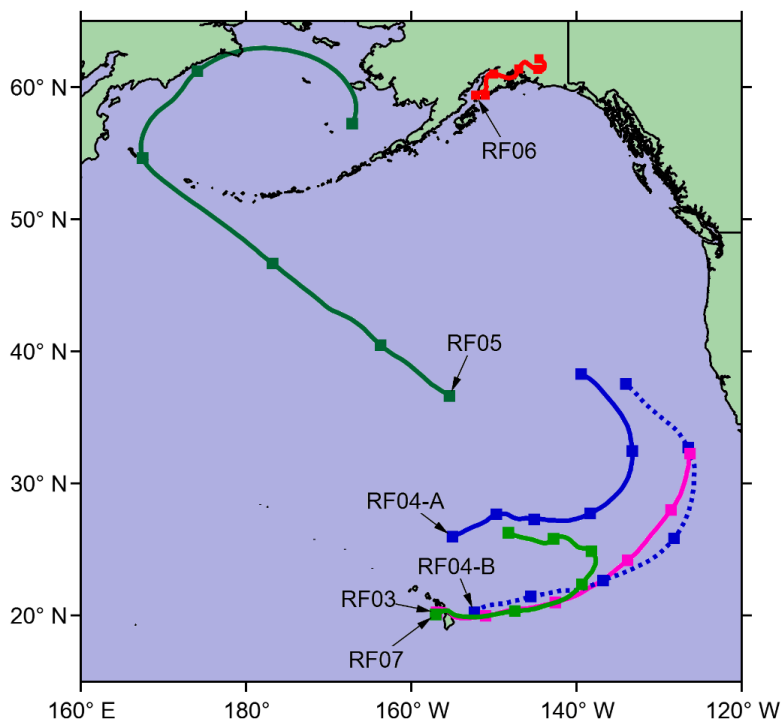
- 620 chemiluminescence fast response analysers, *Atmos Meas Tech*, 3, 163–176,
<https://doi.org/10.5194/AMT-3-163-2010>, 2010.
- Muller, J. B. A., Dorsey, J. R., Flynn, M., Gallagher, M. W., Percival, C. J., Shallcross, D. E., Archibald, A., Roscoe, H. K., Obbard, R. W., Atkinson, H. M., Lee, J. D., Moller, S. J., and Carpenter, L. J.: Energy and ozone fluxes over sea ice, *Atmos Environ*, 47, 218–225, <https://doi.org/10.1016/J.ATMOENV.2011.11.013>, 2012.
- 625 Pearson, R., Jr. and Stedman, D.: Instrumentation for fast-response ozone measurements from aircraft, *Atmos. Technol.*, 12, 51–54, 1980.
- Plake, D., Stella, P., Moravek, A., Mayer, J. C., Ammann, C., Held, A., and Trebs, I.: Comparison of ozone deposition measured with the dynamic chamber and the eddy covariance method, *Agric For Meteorol*, 206, 97–112, <https://doi.org/10.1016/J.AGRFORMET.2015.02.014>, 2015.
- 630 Rannik, Ü., Altimir, N., Mammarella, I., Bäck, J., Rinne, J., Ruuskanen, T. M., Hari, P., Vesala, T., and Kulmala, M.: Ozone deposition into a boreal forest over a decade of observations: Evaluating deposition partitioning and driving variables, *Atmos Chem Phys*, 12, 12165–12182, <https://doi.org/10.5194/ACP-12-12165-2012>, 2012.
- 635 Ridley, B. A. and Howlett, L. C.: An instrument for nitric oxide measurements in the stratosphere, *Review of Scientific Instruments*, 45, 742–746, <https://doi.org/10.1063/1.1686726>, 1974.
- Ridley, B. A., Schiff, H. I., and Welge, K. H.: Measurement of NO in the Stratosphere by NO/O₃ Chemiluminescence (COM-72-10476), 1972.
- 640 Ridley, B. A., Grahek, F. E., and Walega, J. G.: A Small High-Sensitivity, Medium-Response Ozone Detector Suitable for Measurements from Light Aircraft, *J Atmos Ocean Technol*, 9, 142–148, [https://doi.org/https://doi.org/10.1175/1520-0426\(1992\)009%3C0142:ASHSMR%3E2.0.CO;2](https://doi.org/https://doi.org/10.1175/1520-0426(1992)009%3C0142:ASHSMR%3E2.0.CO;2), 1992.
- 645 Rolph, G., Stein, A., and Stunder, B.: Real-time Environmental Applications and Display sYstem: READY, *Environmental Modelling & Software*, 95, 210–228, <https://doi.org/10.1016/J.ENVSOFT.2017.06.025>, 2017.
- Saiz-Lopez, A., Plane, J. M. C. C., Baker, A. R., Carpenter, L. J., von Glasow, R., Gómez Martín, J. C., McFiggans, G., and Saunders, R. W.: Atmospheric Chemistry of Iodine, *Chem Rev*, 112, 1773–1804, <https://doi.org/10.1021/cr200029u>, 2012.
- 650 Stein, A. F., Draxler, R. R., Rolph, G. D., Stunder, B. J. B., Cohen, M. D., and Ngan, F.: NOAA’s HYSPLIT Atmospheric Transport and Dispersion Modeling System, *Bull Am Meteorol Soc*, 96, 2059–2077, <https://doi.org/10.1175/BAMS-D-14-00110.1>, 2015.



- 655 Stella, P., Loubet, B., Lamaud, E., Laville, P., and Cellier, P.: Ozone deposition onto bare soil: A new parameterisation, *Agric For Meteorol*, 151, 669–681, <https://doi.org/10.1016/J.AGRFORMET.2011.01.015>, 2011.
- Torrence, C. and Compo, G. P.: A Practical Guide to Wavelet Analysis, *Bull Am Meteorol Soc*, 79, 61–78, [https://doi.org/10.1175/1520-0477\(1998\)079<0061:APGTWA>2.0.CO;2](https://doi.org/10.1175/1520-0477(1998)079<0061:APGTWA>2.0.CO;2), 1998.
- 660 Vermeuel, M. P., Cleary, P. A., Desai, A. R., and Bertram, T. H.: Simultaneous Measurements of O₃ and HCOOH Vertical Fluxes Indicate Rapid In-Canopy Terpene Chemistry Enhances O₃ Removal Over Mixed Temperate Forests, *Geophys Res Lett*, 48, e2020GL090996, <https://doi.org/10.1029/2020GL090996>, 2021.
- 665 Wohlfahrt, G., Hörtnagl, L., Hammerle, A., Graus, M., and Hansel, A.: Measuring eddy covariance fluxes of ozone with a slow-response analyser, *Atmos Environ*, 43, 4570–4576, <https://doi.org/10.1016/J.ATMOSENV.2009.06.031>, 2009.
- AirChem/FluxToolbox: Collections of scripts for eddy covariance flux calculations (both traditional and wavelet-based): <https://github.com/AirChem/FluxToolbox>, last access: 19 May 2023.
- 670 Wolfe, G. M., Hanisco, T. F., Arkinson, H. L., Bui, T. P., Crounse, J. D., Dean-Day, J., Goldstein, A., Guenther, A., Hall, S. R., Huey, G., Jacob, D. J., Karl, T., Kim, P. S., Liu, X., Marvin, M. R., Mikoviny, T., Misztal, P. K., Nguyen, T. B., Peischl, J., Pollack, I., Ryerson, T., St. Clair, J. M., Teng, A., Travis, K. R., Ullmann, K., Wennberg, P. O., and Wisthaler, A.: Quantifying sources and sinks of reactive gases in the lower atmosphere using airborne flux observations, *Geophys Res Lett*, 42, 8231–8240, <https://doi.org/10.1002/2015GL065839>, 2015.
- 675 Wolfe, G. M., Kawa, S. R., Hanisco, T. F., Hannun, R. A., Newman, P. A., Swanson, A., Bailey, S., Barrick, J., Thornhill, K. L., Diskin, G., DiGangi, J., Nowak, J. B., Sorenson, C., Bland, G., Yungel, J. K., and Swenson, C. A.: The NASA Carbon Airborne Flux Experiment (CARAFE): Instrumentation and methodology, *Atmos Meas Tech*, 11, 1757–1776, <https://doi.org/10.5194/amt-11-1757-2018>, 2018.
- 680 Zahn, A., Weppner, J., Widmann, H., Schlote-Holubek, K., Burger, B., Köhler, T., and Franke, H.: A fast and precise chemiluminescence ozone detector for eddy flux and airborne application, *Atmos. Meas. Tech*, 5, 363–375, <https://doi.org/10.5194/amt-5-363-2012>, 2012.
- 685 Zeller, K.: Summer and autumn ozone fluxes to a forest in the Czech Republic Brdy Mountains, *Environmental Pollution*, 119, 269–278, [https://doi.org/10.1016/S0269-7491\(01\)00176-2](https://doi.org/10.1016/S0269-7491(01)00176-2), 2002.

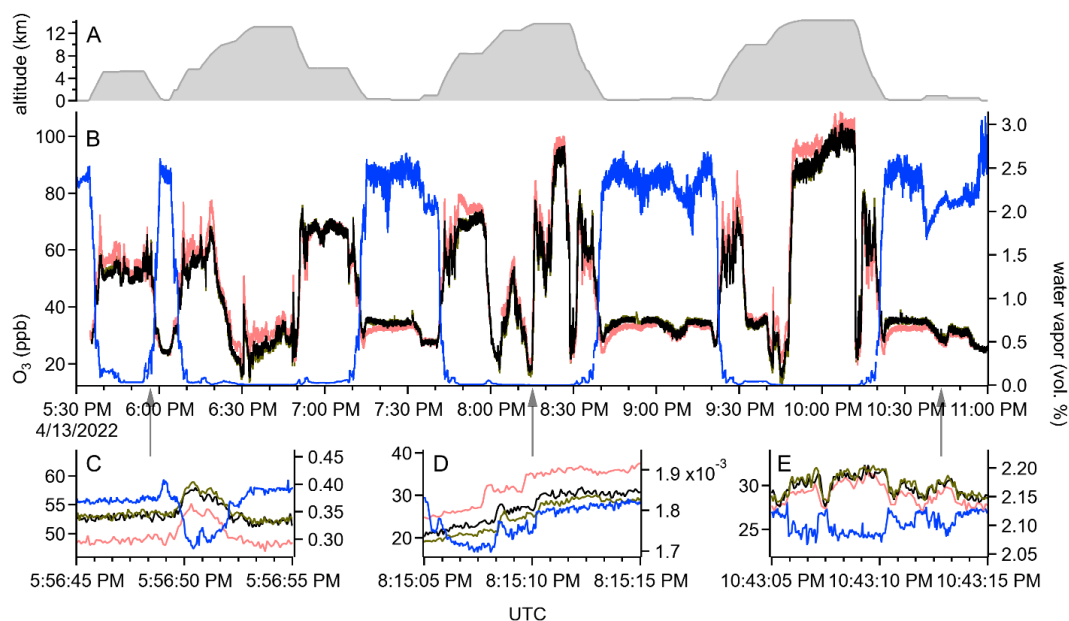


- 690 Zeller, K. F. and Nikolov, N. T.: Quantifying simultaneous fluxes of ozone, carbon dioxide and water vapor above a subalpine forest ecosystem, *Environmental Pollution*, 107, 1–20, [https://doi.org/10.1016/S0269-7491\(99\)00156-6](https://doi.org/10.1016/S0269-7491(99)00156-6), 2000.
- Zhu, Z., Zhao, F., Voss, L., Xu, L., Sun, X., Yu, G., and Meixner, F. X.: The effects of different calibration and frequency response correction methods on eddy covariance ozone flux measured with a dry chemiluminescence analyzer, *Agric For Meteorol*, 213, 114–125, <https://doi.org/10.1016/J.AGRFORMET.2015.06.016>, 2015.
- 695 Zhu, Z., Tang, X., and Zhao, F.: Comparison of Ozone Fluxes over a Maize Field Measured with Gradient Methods and the Eddy Covariance Technique, *Adv Atmos Sci*, 37, 586–596, <https://doi.org/10.1007/S00376-020-9217-4/METRICAL>, 2020.
- 700 Zhu, Z. L., Sun, X. M., Dong, Y. S., Zhao, F. H., and Meixner, F. X.: Diurnal variation of ozone flux over corn field in Northwestern Shandong Plain of China, *Sci China Earth Sci*, 57, 503–511, <https://doi.org/10.1007/S11430-013-4797-9/METRICAL>, 2014.
- Zondlo, M. A., Paige, M. E., Massick, S. M., and Silver, J. A.: Vertical cavity laser hygrometer for the National Science Foundation Gulfstream-V aircraft, *Journal of Geophysical Research Atmospheres*, 115, <https://doi.org/10.1029/2010JD014445>, 2010.

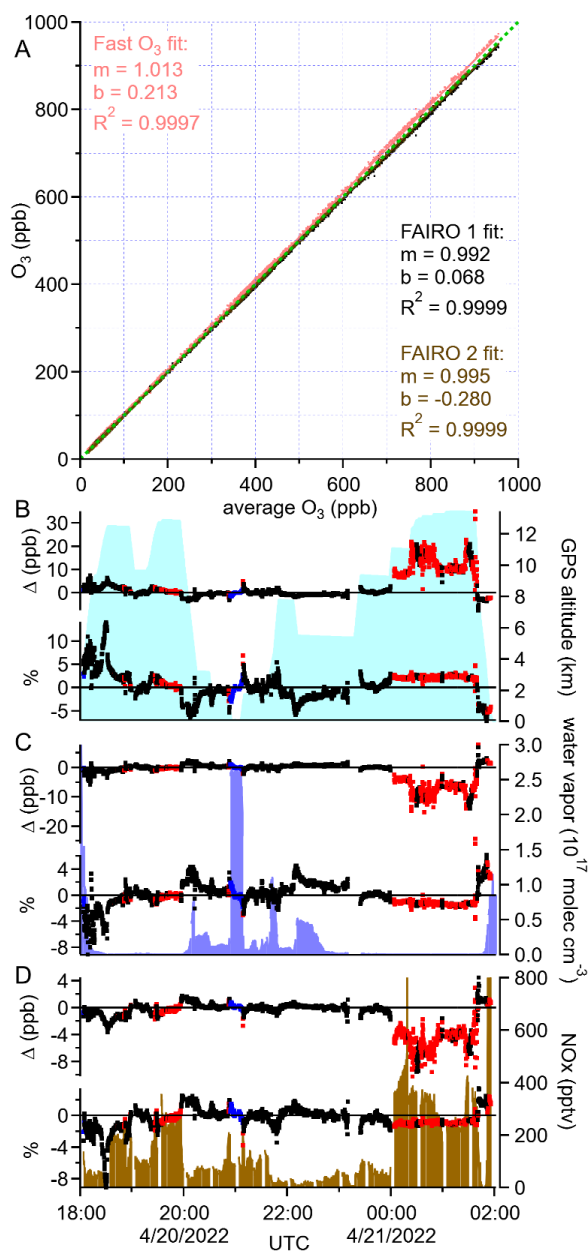


705

Figure 1. Map of flux legs and back-trajectories during TI3GER. Square markers indicate 24-hour periods, and the arrows mark the location of the flux legs.



710 Figure 2. Time stamp synchronization based on the H₂O and O₃ time series. VCSEL data are shown in blue, Fast O₃ data in salmon, FAIRO 1 in black, and FAIRO 2 in dark olive. All traces are shown at the native instrument resolution (25 Hz for VCSEL, 12.5 Hz for the FAIROs, and 10 Hz for Fast O₃). A: altitude time series. B: time series for the entire flight. C-E: Zooms to cross-covariance events with gray arrows pointing to exact times.



715 Figure 3. A: Aggregated data from RF03-07 with fits relative to global average; one-to-one line in green. Absolute and relative differences from average during RF05 for Fast O₃ in Panel B; FAIRO 1 in Panel C; and FAIRO 2 in Panel D. Background shading for GPS altitude in Panel B, VCSEL in Panel C, and NO_x in Panel D.

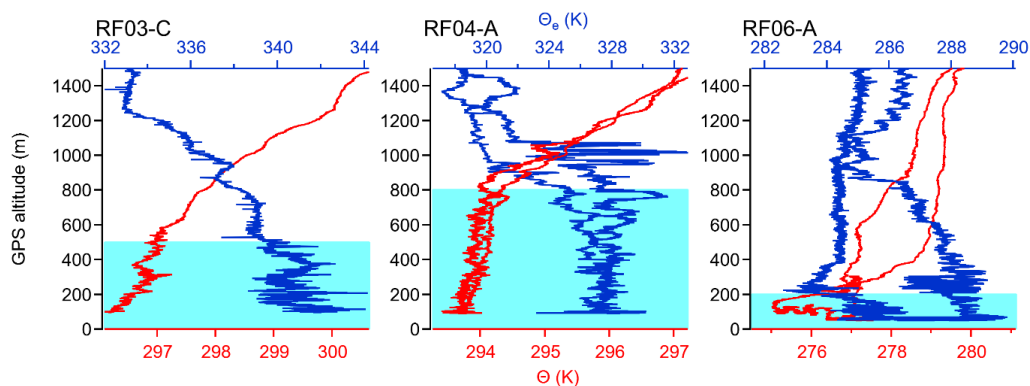
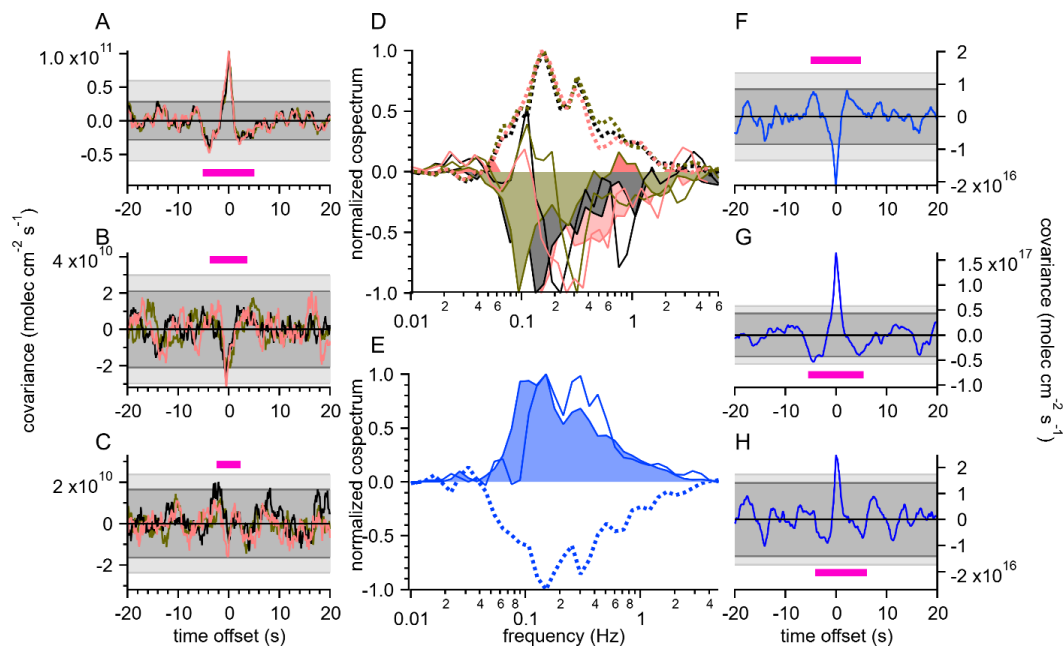
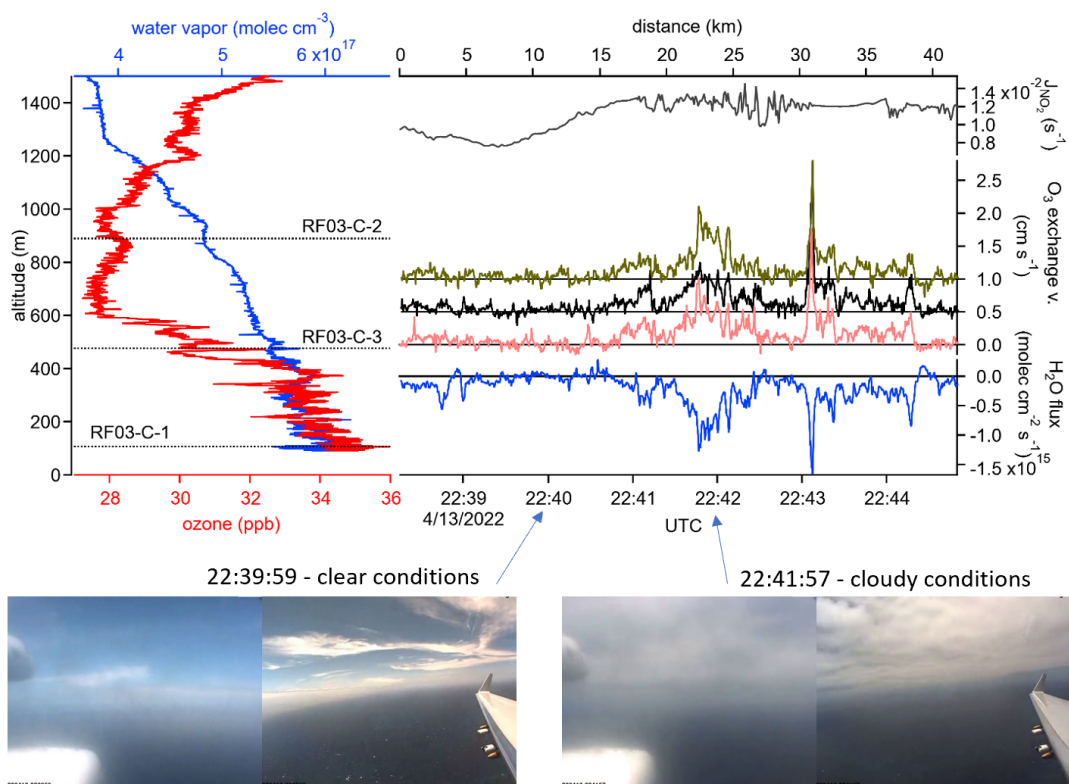


Figure 4. Representative potential temperature and equivalent potential temperature profiles for determining MBL height in three different flux legs. The MBL is shown as light blue shading.



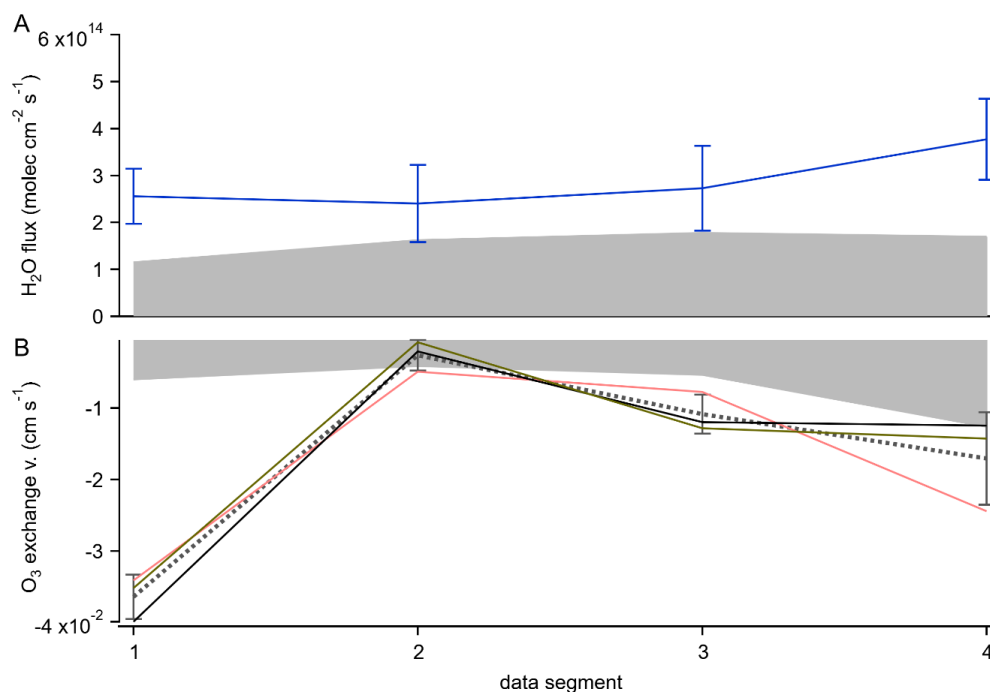
720

Figure 5. Cross-covariance plots for RF03-C-2 (A), RF04-A-1 (B), and RF06-A-1 (C), and their respective water vapor fluxes (F-H). Normalized cospectra are shown in D and E. For ozone data, Fast O3 is shown in salmon, FAIRO 1 in black, and FAIRO 2 in olive. In Panels D and E, RF03 is shown as a dotted line, RF04 as a shade to zero, and RF06 as a solid line. Integral time scales are shown as fuchsia bars.



725

730 Figure 6. Ozone and water vapor vertical profiles and time series for EC fluxes from the RF03-C leg. Ozone profile is the average of all three instruments. Dashed lines indicate flight altitudes. Right: J_{NO_2} in gray, fluxes from Fast O₃ (salmon), FAIRO 1 (black), FAIRO 2 (olive), and VCSEL (blue). Vertical offsets of 0.5 cm s^{-1} and 1 cm s^{-1} have been added to FAIRO 1 and 2 to better illustrate the close agreement between the three O₃ instruments. Images of the webcams from RF03 flight movies illustrate cloud cover conditions.



735 Figure 7. Segments of RF06-A-1. Panel A: VCSEL is shown in blue. Error bars represent modified Langford RE_{RMSE}. Panel B: FO3 in salmon, FAIRO 1 in black, and FAIRO 2 in dark olive. The average is shown as the dotted line. Error bars represent standard deviation. In both panels, the 95% LOD is shaded. Each data segment is 75 seconds long.

flight	average (ppb)	max (ppb)	FO3 slope	FO3 offset (ppb)	F1 slope	F1 offset (ppb)	F2 slope	F2 offset (ppb)
RF03	47.4	103	1.028	0.44	0.982	0.02	0.990	-0.46
RF04	76.5	409	1.029	-0.03	0.981	0.24	0.989	-0.21
RF05	172.8	955	1.024	-1.40	0.985	1.10	0.991	0.34
RF06	223.0	887	1.000	0.15	0.998	0.15	0.998	-0.30
RF07	78.6	177	1.014	0.08	0.992	-0.04	0.994	-0.04

Table 1. Linear fit parameters of individual instruments to average.



exchange velocity (cm s^{-1})

Leg Code	Date UTC	Start UTC	End UTC	location	alt (m)	Fast O3	FAIRO 1	FAIRO 2	average	st. dev.
RF03-A-1	4/13/2022	19:16:43	19:20:13	off SW coast of HI	312	+0.037	+0.020	+0.015	+0.024	0.012
RF03-B-1	4/13/2022	20:45:33	20:52:08	off SW coast of HI	101	+0.033	+0.014	+0.003	+0.017	0.015
RF03-C-2	4/13/2022	22:38:15	22:44:51	off SW coast of HI	889	+0.131	+0.135	+0.136	+0.134	0.003
RF03-C-3	4/13/2022	22:46:02	22:54:15	off SW coast of HI	476	+0.099	+0.093	+0.100	+0.097	0.004
RF04-A-1	4/15/2022	21:16:20	21:21:46	North of HI	93	-0.042	-0.037	-0.030	-0.036	0.006
RF04-A-2	4/15/2022	21:22:12	21:25:50	North of HI	101	-0.030	-0.014	-0.017	-0.021	0.008
RF06-A-1	4/21/2022	19:39:47	19:44:44	off AK coast	58	-0.015	-0.008	-0.009	-0.010	0.004
RF06-B-1	4/22/2022	02:28:59	02:32:01	halfway between AK and HI	116	+0.022	+0.024	+0.024	+0.023	0.001
RF07-A-1	4/23/2022	21:43:30	21:49:20	west of HI airport	116	-0.017	-0.013	-0.014	-0.015	0.002
RF07-A-3	4/23/2022	22:04:07	22:06:45	west of HI airport	778	-0.012	-0.015	-0.015	-0.014	0.002
RF07-A-4	4/23/2022	22:11:24	22:16:08	west of HI airport	472	-0.035	-0.029	-0.036	-0.033	0.004

Table 2. Summary of ozone EC flux results.